Chemical Engineering Journal 437 (2022) 135289

Contents lists available at ScienceDirect

Chemical Engineering Journal

journal homepage: www.elsevier.com/locate/cej

Engineering nanocomposite metal-phenolic network membranes with hollow MOFs via *in-situ* etching for High-efficiency organic solvent nanofiltration

Yizhou Chen [a], Yuting Bai [a], Lijun Meng [c], Wenting Zhang [a], Jingjing Xia [a], Zhiming Xu [a], Rui Sun [a], Yan Lv [a,b,*], Tianxi Liu [a,b,*]

[a] State Key Laboratory for Modification of Chemical Fibers and Polymer Materials, Innovation Center for Textile Science and Technology, College of Materials Science and Engineering, Donghua University, 2999 North Renmin Road, Shanghai 201620, PR China
[b] Key Laboratory of Synthetic and Biological Colloids, Ministry of Education, School of Chemical and Material Engineering, Jiangnan University, Wuxi 214122, PR China
[c] State Key Laboratory of Pollution Control and Resource Reuse, Shanghai Institute of Pollution Control and Ecological Security, School of Environmental Science and Engineering, Tongji University, Shanghai 200092, PR China

ARTICLE INFO

Keywords:
Thin-film nanocomposite membrane
Metal-phenolic networks
Hollow metal-organic frameworks
In-situ etching
Organic solvent nanofiltration

ABSTRACT

Organic solvent nanofiltration (OSN), as an emerging membrane separation technology, holds great potential in pharmaceutical and chemical applications. However, the development of such a promising technology is severely retarded by the trade-off between permeability and selectivity. Herein, we report a novel thin-film nanocomposite (TFN) membrane by incorporating hollow metal-organic frameworks (MOFs) into the metal-phenolic network (MPN) selective layer for highly efficient OSN. This nanocomposite selective layer is fabricated via an aqueous deposition of tannic acid (TA) and Fe^{II} ions with MOFs, during which the MOFs are *in-situ* etched to a hollow structure. Attributed to the extra transfer channels provided by hollow MOFs, the methanol permeance of the TFN membranes increases to 24.7 $L{\cdot}m^{-2}{\cdot}h^{-1}{\cdot}bar^{-1}$, exhibiting an improvement of 270% compared with the membranes without MOFs (9.1 $L{\cdot}m^{-2}{\cdot}h^{-1}{\cdot}bar^{-1}$). Meanwhile, the coordination interaction between TA and metal centers in MOFs endows excellent interfacial compatibility between MPN matrix and MOF fillers, guaranteeing a defect-free selective layer and thus high rejection for small organic molecules (>99% for Alcian blue). Furthermore, various MOFs, including ZIF-67, prussian blue (PB), and MIL-53(Al), are also employed to fabricate MPN/MOF nanocomposite membranes, proving the availability and universality of this facial aqueous deposition strategy. Additionally, we also take deep insight into the mechanism of *in-situ* etching based on the density functional theory (DFT) calculation to pave the way for the fabrication of TFN membranes with other hollow nanofillers. This work provides a sufficient strategy for the design and construction of novel highly efficient OSN nanocomposite membranes with excellent permeability and retention performance.

1. Introduction

In the past, conventional separation processes including distillation, evaporation, and adsorption, were mainly employed for the purification and recovery of organic solvents in pharmaceutical and chemical industries. [1,2] Nowadays, membrane separation technology, especially the organic solvent nanofiltration (OSN), has emerged as an attractive alternate due to its high selectivity, low energy consumption, minimized thermal damage for heat-sensitive molecules and good environmental compatibility. [3,4] The current OSN membranes such as polyimide (PI) membrane and polyamide (PA) membrane reveal good retention performance and stability in various organic solvents. [4,5] However, the trade-off effect between selectivity and permeability is restricting the separation efficiency of these OSN membranes severely, which remains a significant challenge for the development and applications of OSN membranes. [6–8]

Doping porous nanofillers into polymeric selective layers of the OSN membranes is considered as an effective strategy to alleviate the trade-off effect. [9–17] Metal-organic frameworks (MOFs), one kind of organic-inorganic hybrid material, has been widely adopted due to their

* Corresponding authors at: State Key Laboratory for Modification of Chemical Fibers and Polymer Materials, Innovation Center for Textile Science and Technology, College of Materials Science and Engineering, Donghua University, 2999 North Renmin Road, Shanghai 201620, PR China.
E-mail addresses: yanlv@dhu.edu.cn (Y. Lv), txliu@dhu.edu.cn (T. Liu).

https://doi.org/10.1016/j.cej.2022.135289
Received 3 January 2022; Received in revised form 5 February 2022; Accepted 13 February 2022
Available online 16 February 2022

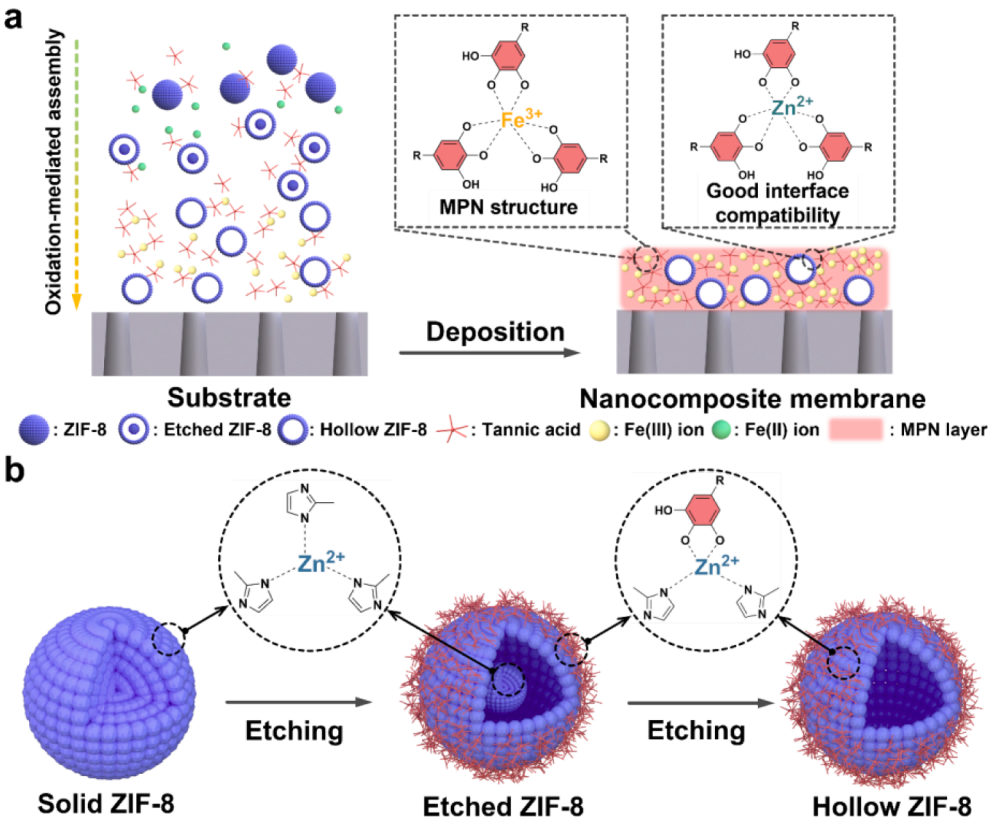

Fig. 1. Schematic illustration of (a) the fabrication process for MPN/MOF nanocomposite membranes and (b) the etching process of ZIF-8.

compatibility with polymers and the highly tunable porous topologies. [18–23] For instance, Livingston *et al.* have introduced various MOFs, including ZIF-8, MIL-53(Al), NH_2-MIL-53(Al) and MIL-101(Cr), into PA layer to enhance the methanol permeability effectively. [24] However, the agglomeration of MOF nanoparticles and the inadequate interfacial interaction with the polymer matrix would lead to non-selective voids, resulting in declined selectivity and structural instability. Plenty of efforts have been devoted to solve these problems.[25–28] Jin *et al.* modified the MOFs with polydopamine, achieving improved dispersibility in aqueous solution and better affinity with the PI matrix. [29] Natural plant polyphenols, such as tannic acid (TA), ellagic acid (EA) and gallic acid (GA), are emerging to be applied to decorate the MOFs due to their universal adhesive property, good hydrophilicity and the chelation ability with metal ions in MOFs. [30] Li and co-workers demonstrated that PA membranes containing TA modified ZIF-8 nanoparticles presents much improved aqueous nanofiltration performance both in the water permeance and salt rejection compared with the membranes comprised unmodified ZIF-8 nanoparticles. [31] On the one hand, TA could adhere to the surface of ZIF-8 nanoparticles via coordination, benefiting for the dispersion of ZIF-8 in aqueous solutions as well as their compatibility with the PA matrix. More importantly, ZIF-8 nanoparticles can be etched into hollow structures by TA. This would decrease the mass transfer resistance of nanocomposite selective layers significantly, ascribed to the additional transfer channels and the much shortened transfer distance inside the ZIF-8 nanoparticles. [32–34] However, the MOFs need to be pre-modified in these cases, making it complicated for the fabrication of the TFN membranes. Therefore, it is urgent to develop a more facile and straightforward method to construct novel high-performance TFN membranes.

Metal phenolic networks (MPNs) are a kind of versatile and substrate-independent coatings, composed of metal centers (*e.g.* Fe^{III}) coordinating with phenolic ligands (*e.g.* TA). [35,36] In recent years, MPN has been expected as selective layers constructed on ultrafiltration substrates to separate small organic molecules (*e.g.* dyes) due to its theoretical pore size of several to sub nanometers. [37] Though several works on TA-Fe^{III} MPN nanofiltration membranes have been reported, the performances were far from satisfaction since the pore size of the prepared TA-Fe^{III} layer was much larger than the ideal situation. [38–42] This is mainly because the rapid and uncontrollable assembly of TA-Fe^{III} complexes will inevitably cause irreversible defects and voids in the TA-Fe^{III} layer, leading to loose and incomplete structures. [43] Choi and Caruso's group claimed that utilizing Fe^{II} ions instead of Fe^{III} ions in aqueous solutions to react with TA could not only reduce the assembly rate but also realize the self-correction of MPN structures. [43,44] As a result, the pore size of MPN films formed by Fe^{II} can be reduced to about 2 nm while that of TA-Fe^{III} film is above 6 nm. [44] Inspired by the reported works, we propose a one-step aqueous deposition approach to fabricate novel MPN nanocomposite membranes for high-efficiency OSN. Herein, the membrane is fabricated by immersing ultrafiltration substrates in a simple mixed aqueous solution of TA and $FeCl_2$ containing MOFs. After deposition, a defect-free nanocomposite MPN layer with *in-situ* etched hollow MOFs is formed on the substrate (Fig. 1). The hollow MOFs doped in the MPN matrix can provide adequate mass transfer channels to reduce the transmembrane resistance and thus improve the permeability for various solvents sufficiently without sacrificing the rejection performance. This can be ascribed to the elimination of non-selective voids by the good interface compatibility between MPN matrix and MOFs, which is derived from multi-interaction among TA and MPN matrix or MOFs including covalent/noncovalent interaction and the coordination interaction. Attributed to the synergy of the hollow MOFs and the defect-free structure of MPN layer, the prepared membranes achieve excellent permeability accompanied with high selectivity for various molecules during the OSN process.

2. Experiments

2.1. Materials

Tannic acid (TA) and 1,4-benzene dicarboxylic acid (BDC) were purchased from Sigma-Aldrich. $FeCl_2{\cdot}4H_2O$, $Zn(NO_3)_2{\cdot}6H_2O$, $CoCl_2{\cdot}6H_2O$, $Al(NO_3)_3{\cdot}9H_2O$, 2-methylimidazole (mIm), glutaraldehyde (GA, 50% aqueous solution) and polyethylene glycol (PEG) with different molecular weights (Mw = 300, 600, 1000, 2000, 4000 Da) were purchased from Sinopharm Chemical Reagent Co., Ltd. Alcian blue (AB) and rose bengal (RB) were obtained from Rhawn Chemical Reagent Co., Ltd. Methyl orange (MO), orange G (OG), brilliant blue (BB), $K_4Fe(CN)_6{\cdot}3H_2O$ and polyvinyl pyrrolidone (PVP, K23-K27) were purchased from Aladdin Industrial Co., Ltd. All organic solvents were supplied by Shanghai Chemical Reagent Co., Ltd. Polyacrylonitrile ultrafiltration membranes (PAN, MWCO = 200,000 Da) were got from Ande membrane separation technology engineering (Beijing) Co., Ltd. Deionized (DI) water (pH = 6) was produced by a Purifier water purification system.

2.2. Synthesis and modification of MOFs

To synthesis ZIF-8, $Zn(NO_3)_2{\cdot}6H_2O$ (9.87 mmol) and mIm (79.04 mmol) were dissolved in methanol at first, respectively. Then, the Zn $(NO_3)_2$ solution was rapidly poured into the mIm solution under room temperature with stirring (500 rpm). The mixed solution was kept for 30 min to obtain ZIF-8 nanoparticles with a diameter of about 30 nm. After that, ZIF-8 was centrifuged from the solution and washed thoroughly with methanol for more than three times. Finally, the obtained ZIF-8 nanoparticles were dried at 70 °C overnight in the oven. [45]

ZIF-67, [46] prussian blue (PB), [47] and MIL-53(Al) [24] nanoparticles were synthesized according to the reported methods.

For TA modification and etching, the MOFs (12 mg) were dispersed in 30 ml TA (240 mg) aqueous solution under ultrasonication, and adjusted the pH value of the solution to 3.5 after 10 min. The etched MOFs were collected by centrifugation and washed by DI water and methanol for three times. The modified MOFs were denoted as ZIF-8/TA, ZIF-67/TA, PB/TA and MIL-53(Al)/TA, respectively.

2.3. Preparation of nanocomposite membranes

A designed amount of the synthesized MOFs was dispersed in 30 ml TA (240 mg) aqueous solution, the pH value of which was then adjusted to 3.5. The PAN membrane was pre-wetted by 50% ethanol solution and immersed in MOF/TA solution for 5 min to ensure the pre-anchoring of TA on membrane surface. After that, 30 ml $FeCl_2{\cdot}4H_2O$ (294 mg) aqueous solution was mixed into the MOF/TA solution to trigger the assembly and deposition of MPN onto the PAN substrate. After deposited for designed time, the obtained MPN/MOF nanocomposite membrane was rinsed with DI water thoroughly. Finally, the nanocomposite membrane was cross-linked by a GA (10 wt%) solution at 30 °C for 3 h to further improve the organic solvent resistance property. The nanocomposite membranes with ZIF-8 loading of 0 wt%, 0.01 wt%, 0.02 wt %, 0.03 wt% and 0.04 wt% were denoted as MPN, MPN/ZIF-8–1, MPN/ZIF-8–2, MPN/ZIF-8–3 and MPN/ZIF-8–4, respectively.

2.4. Characterization

The morphologies of MOFs and membranes were observed using field emission scanning electron microscopy (FE-SEM, JEOL-7500F, Hitachi, Japan), transmission electron microscopy (TEM, JEM-2100, Hitachi, Japan) and atomic force microscopy (AFM, MFP-3D Bio, USA). The cross-section sample of the membrane for TEM was sliced by an ultrathin slicer (LEICA EM UC7, Germany) at room temperature. The chemical structures of MOFs and membrane surfaces were characterized by X-ray photoelectron spectroscopy (XPS, Escalab-250Xi, USA), attenuated total reflectance flourier transform infrared spectroscopy (ATR-FTIR, NEXUS-670, USA) and energy-dispersive X-ray spectroscopy (EDX). The crystal structure of MOFs was analyzed by using a powder X-ray diffraction (XRD, DX-2700B, China). Specific surface area measurements of MOFs was performed according to the BET (Brunauer-Emmett-Teller) method based on the N_2 adsorption/desorption experiment (Micromeritics ASAP-2460, USA). The zeta potential of MOFs was measured by using a zeta potential analyzer (Andon paar Litersizer-500, Austria). The water contact angle of MOFs was measured by a dynamic contact angle testing instrument (OSA200, Germany). The concentration of dye solutions was determined according to the standard curve measured by an ultraviolet–visible spectrophotometer (UV-vis, PERSEE TU-1901, China).

2.5. Evaluation of nanofiltration performance

The evaluation of OSN performance was carried out in a dead-end cell (Sterlitech, USA) at 25 °C with constant stirring speed of 500 rpm. The effective filtration area was 14.6 cm^2. After pre-soaked in organic solvent overnight, the membrane was put into the testing cell aligning with the O-ring. Then, the pure organic solvent was filled and the membrane was pre-compacted under a pressure of 5 bar for 30 min. For testing, different dye solutions (50 mg/L) were added as feed into the cell and the pressure was fixed at 4 bar..

The permeance (J) is determined by measuring the permeate volume (V) per unit area (A) per unit time (t) under per unit applied pressure(ΔP) according to the following equation (1).

$$J = \frac{V}{A{\cdot}t{\cdot}\Delta P} \tag{1}$$

The solute rejection rate (R) is calculated from equation (2), where C_p and C_f are the concentration of the permeate and feed solutions, respectively.

$$R(\%) = \left(1 - \frac{C_p}{C_f}\right) \times 100 \tag{2}$$

The applied pressure was gradually increased from 2 bar to 8 bar to evaluate the structure and performance stability of the nanocomposite membranes in further. And each of the applied pressure was kept for 30 min before testing.

2.6. Measurement of membrane pore size and distribution

The pore size and distribution of the membrane was determined by the molecular probe method. PEGs with various molecular weights were used as molecular probes. The Stokes radii (r) of PEG can be calculated from equation (3), where M_w is the molecular weight.

$$r = 16.73 \times 10^{-10} \times M_W^{0.557} \tag{3}$$

The normal distribution of membrane pore size can be calculated by substituting the pore diameter of the membrane (d_p), the geometric mean radius of the PEG at the rejection rate of 50% (μ_p), and the geometric standard deviation about μ_p (σ_p) into equation (4), ignoring the effects of the steric and hydrodynamic of the pore on solute rejection. [48] It needs to be further explained that σ_p is defined as the ratio of PEG radius at R = 84.13% to that of R = 50%.

$$\frac{dR(d_p)}{dd_p} = \frac{1}{d_p ln\sigma_p\sqrt{2\pi}}\, exp\left(-\frac{\left(lnd_p - ln\mu_p\right)^2}{2\left(ln\sigma_p\right)^2}\right) \tag{4}$$

2.7. Simulation

The coordination simulation between organic ligands and metal ions was carried out with Gaussian16 software through density functional theory (DFT) approach. As TA can be considered as a series of

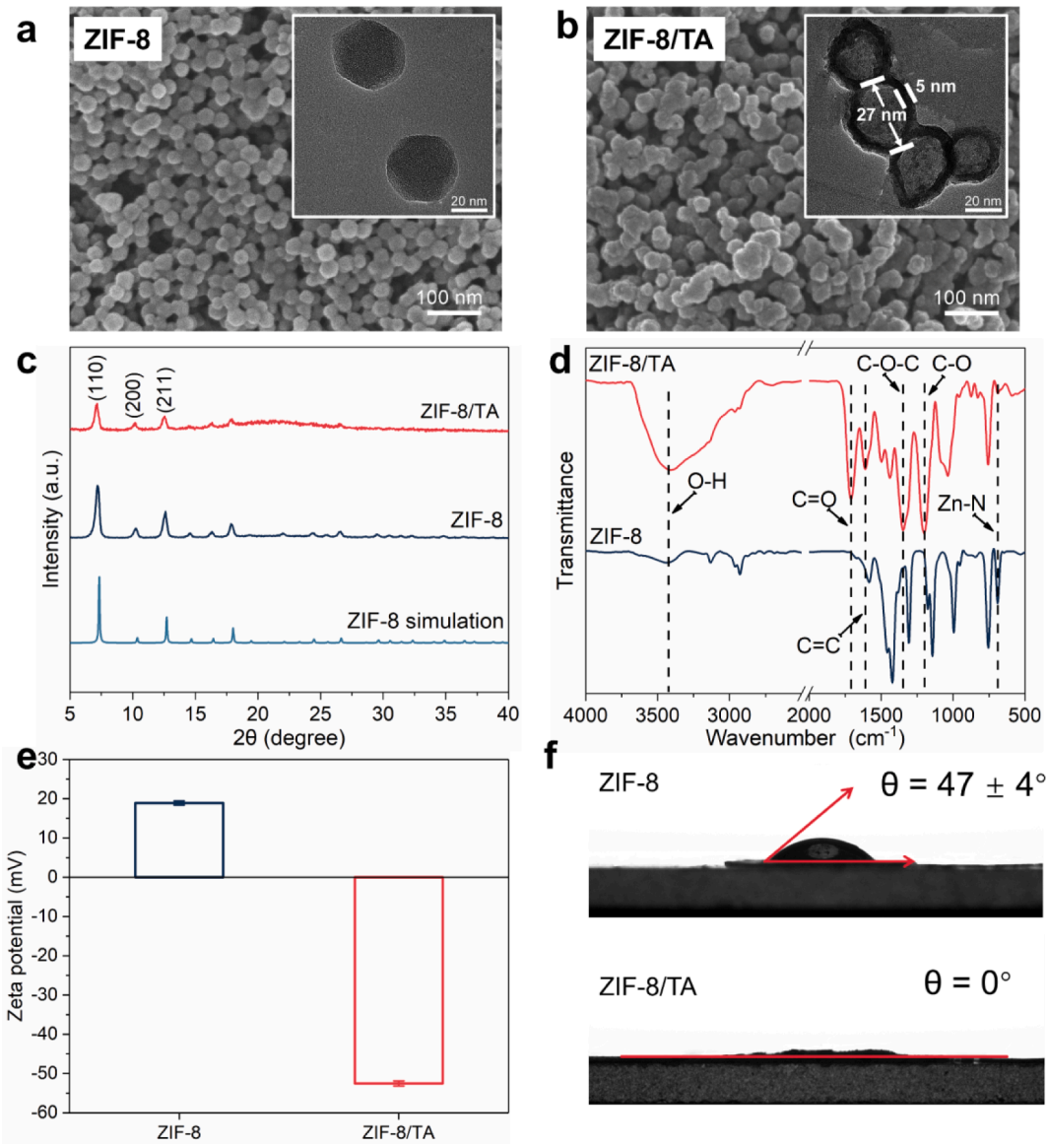

Fig. 2. SEM images of (a) ZIF-8 and (b) ZIF-8/TA nanoparticles. The insets are corresponding TEM images. (c) XRD spectra, (d) FTIR spectra, (e) surface zeta potentials and (f) water contact angles of the synthesized ZIF-8 and ZIF-8/TA.

polygalloyl glucose molecules with different degrees of esterification, gallic acid was used in simulations as the basic building block of TA. The structures were optimized at the B3LYP/6-311G(d) level and the electronic energies were calculated with larger basis sets of 6-311+G(d,p). [49–51] The D3(BJ) empirical dispersion correction was adopted to ensure the results accurate. [52] The binding energy ($\Delta E_{binding}$) between the organic ligand and metal ion was calculated as follows:

$$\Delta E_{binding} = E_{(organic\ ligand/metal\ ion)} - (E_{(organic\ ligand)} + E_{(metal\ ion)}) \quad (5)$$

The $E_{(organic\ ligand/metal\ ion)}$ is defined as the energy of organic ligand/metal ion coordination complexes. The $E_{(organic\ ligand)}$ and the $E_{(metal\ ion)}$ are defined as the energy of deprotonated organic ligands and metal ions, respectively.

3. Results and discussion

Fig. 2a and b show the morphology of ZIF-8 before and after TA modification. The synthesized ZIF-8 exhibits a diameter of about 30 nm with narrow size distribution. After modification, the surface of ZIF-8/TA nanoparticles becomes crude. Moreover, the TEM image of ZIF-8/TA reveals a hollow structure with a shell thickness of about 5 nm, demonstrating the successful etch by TA (Fig. 2b). Ascribed to the eliminated inner mesoporous structure, the specific surface area of ZIF-8/TA nanoparticles decreases significantly compared with the pristine ZIF-8 samples (Figure S1). However, the XRD spectrum of ZIF-8/TA maintains diagnostic diffraction peaks at 7.34° (110), 10.38° (200) and 12.72° (211), which are consistent with that of the synthesized and standard ZIF-8 crystals (Fig. 2c). The chemical structures of ZIF-8 and ZIF-8/TA nanoparticles were further characterized by ATR-FTIR and XPS. Compared with ZIF-8, new characteristic peaks appear at 1708 cm^{-1} and 1349 cm^{-1} in the spectrum of ZIF-8/TA, corresponding to the C=O vibration and the C-O-C vibration in ester groups (Fig. 2d). The broad O-H vibration peak is significantly enhanced at 3200-3500 cm^{-1} for ZIF-8/TA ascribed to the abundant hydroxyl groups in TA. Moreover, the Zn-N vibration peak at 690 cm^{-1} is weakened significantly as the surface of ZIF-8 is covered by TA. This is also proved by the XPS results, where the O/N ratio reaches to 5.68 for ZIF-8/TA while the atomic percent of Zn element declines to 3.09 % compared with that of ZIF-8 samples (Figure S2). Additionally, the surface of ZIF-8/TA nanoparticles becomes negatively charged accompanied with improved hydrophilicity

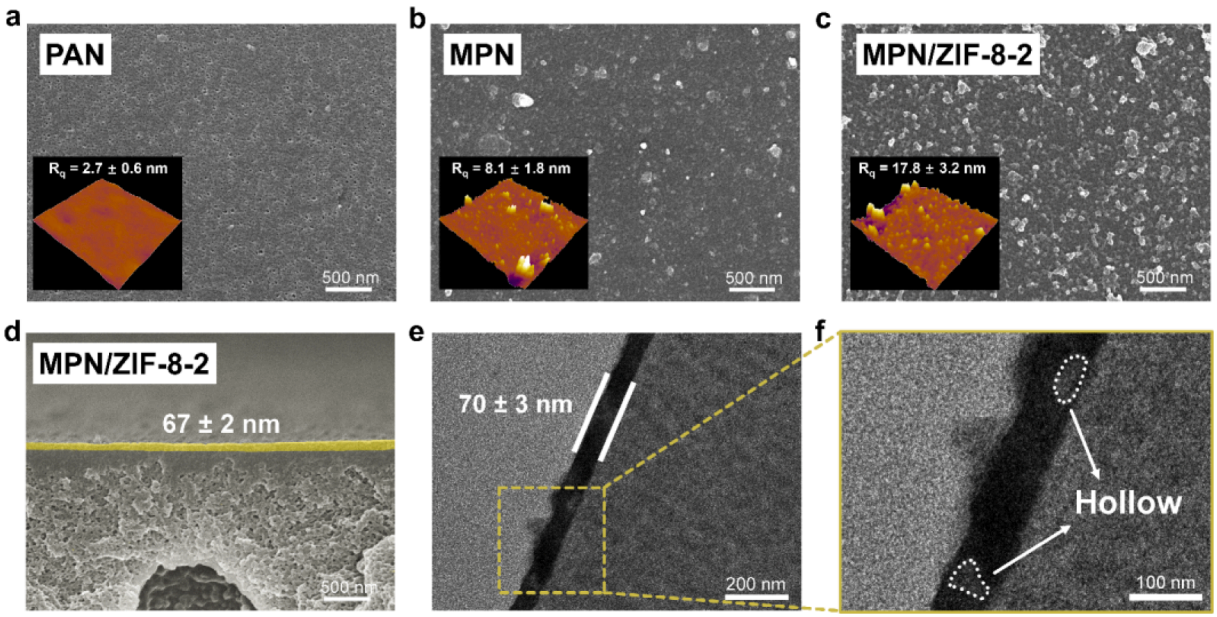

Fig. 3. SEM images of (a) PAN, (b) MPN, and (c) MPN/ZIF-8-2 membrane surfaces. The inserts are corresponding AFM images. (d) SEM and (e, f) TEM images for the cross-section of the MPN/ZIF-8-2 membrane.

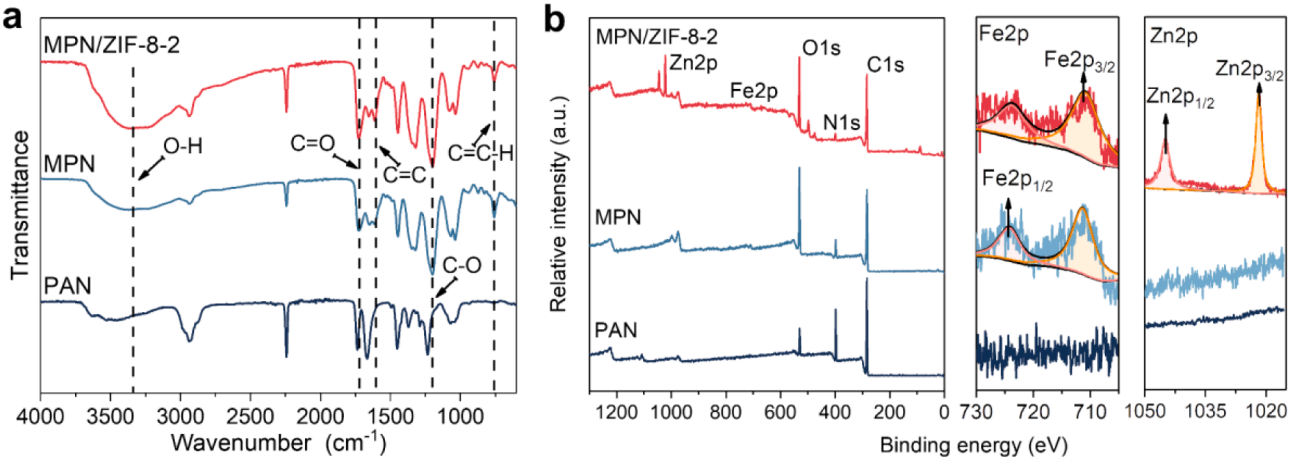

Fig. 4. (a) ATR-FTIR and (b) XPS spectra of PAN, MPN and MPN/ZIF-8–2 membranes.

(Fig. 2e and 2f) after modification, benefiting for their homogeneous dispersion in aqueous solutions and the resultant MPN matrix.

The MPN TFC membranes were prepared via an aqueous deposition of TA and Fe^{II} ions. As shown in Figure S3, the pores on PAN substrate can be covered gradually by the MPN film with deposition time increasing. Meanwhile, globular structure can be observed on the membrane surface when deposition time is prolonged due to the growth and adhesion of TA-Fe^{II} complexes. The cross-section morphology of MPN membranes indicates that the thickness of the MPN layer can be tailored from 0 to about 90 nm by adjusting the deposition time (Figure S3 and S4). The MPN nanocomposite membranes were prepared by introducing ZIF-8 nanoparticles into the TA solutions. As can be seen from Fig. 3a-c, the PAN substrate surface is relatively smooth with a roughness of about 2.7 nm. After MPN deposition, some nodules appear on the membrane surface with increased roughness of around 8.7 nm. The surface of MPN/ZIF-8-2 membrane becomes much rougher (R_q = 17.8 nm) than the MPN membrane with lots of nodules, as the ZIF-8 nanoparticles could promote the growth of TA-Fe^{II} complexes by acting as nucleus. The cross-section morphology of MPN/ZIF-8–2 membrane was observed by SEM and TEM (Fig. 3d-f). Fig. 3d reveals that the MPN/ZIF-8 layer adheres to the PAN substrate robustly without obvious boundary, indicating good interfacial compatibility, which is conducive to the structural stability of composite membranes. The TEM image exhibits a dense MPN/ZIF-8-2 layer on the PAN substrate with a thickness of about 70 nm (Fig. 3e). In addition, hollow ZIF-8 nanoparticles can be observed in the MPN/ZIF8-2 layer, proving the successful construction of the designed nanocomposite membranes (as marked in Fig. 3f).

ATR-FTIR and XPS were also conducted to verify the chemical structures of different membranes. As shown in Fig. 4a, characteristic peaks appear at 1708 cm^{-1}, 1200 cm^{-1} and 790 cm^{-1} in the ATR-FTIR spectrum of MPN and MPN/ZIF-8-2 membranes, corresponding to the C=O stretching vibration, the C-O stretching vibration and the aromatic C-H deformation vibration from TA, respectively. From the XPS spectra, it can be indicated that the successful formation of the MPN layer by the increased atomic percent of O element compared with the PAN substrate, and the new peak of Fe element for MPN and MPN/ZIF-8-2 membranes. Furthermore, Zn element appears on the surface of MPN/ZIF-8-2 membranes, confirming the incorporation of ZIF-8 in MPN layers (Fig. 4b).

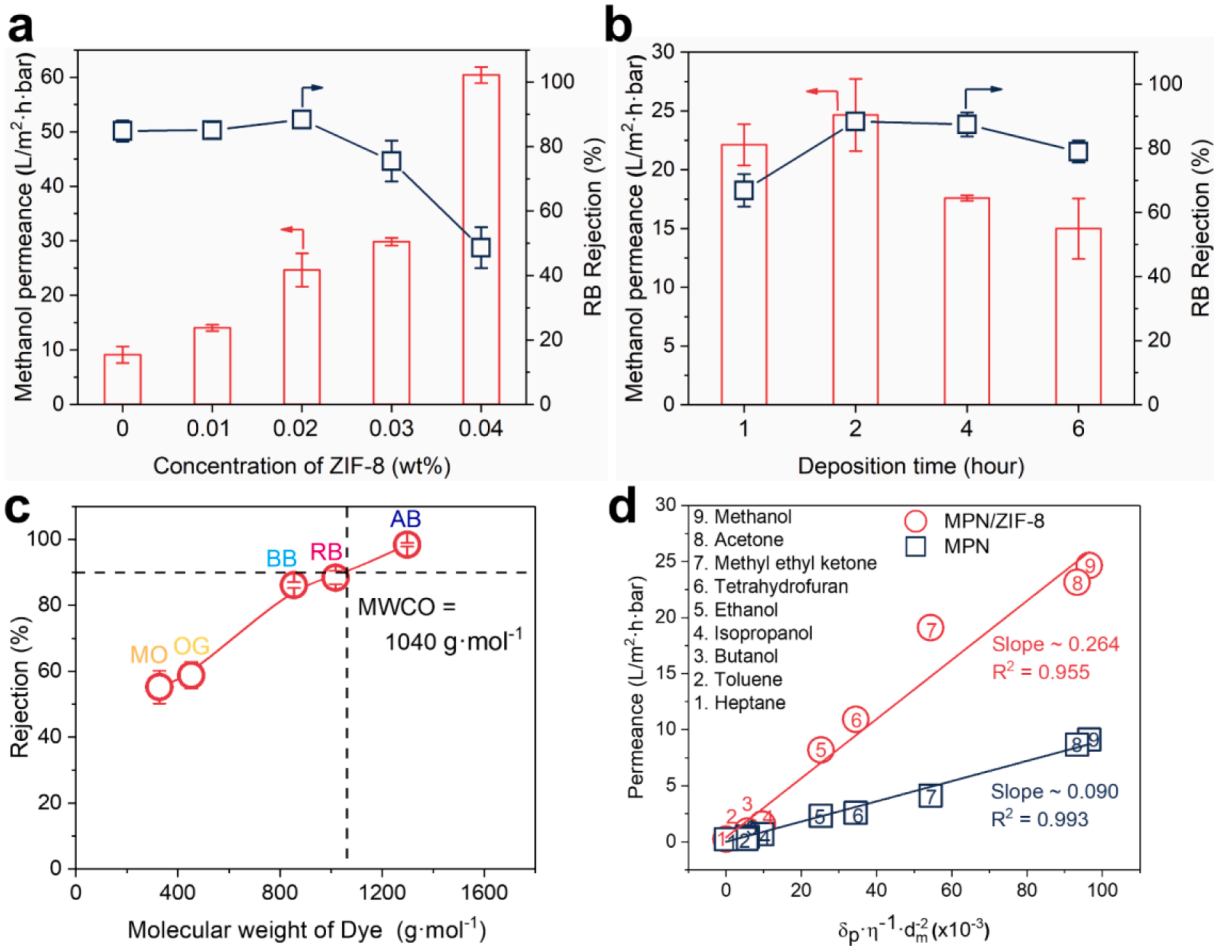

Fig. 5. Effects of (a) ZIF-8 loading amount and (b) deposition time on OSN performances of MPN/ZIF-8 membranes. RB in methanol solutions (50 mg/L) is used as feed. (c) The rejections of the MPN/ZIF-8-2 membrane for different dyes. Methanol solutions (50 mg/L) containing different dyes are used as feeds. (d) Relationship of the solvent permeance against the combined solvent properties (viscosity, molar diameter, and solubility parameter) for the MPN/ZIF-8-2 membrane.

The prepared nanocomposite membranes exhibit excellent stability in a variety of protonic and aprotic organic solvents (Figure S5). This should be attributed to the high stability constant of TA-Fe^{III} complexes and the covalent crosslinking of MPN by GA (Figure S6). [53] Therefore, these nanocomposite membranes are expected to be applied in OSN. First of all, the effects of ZIF-8 amount and deposition time on membrane performance are investigated in view of their significant impact on the membrane structure and property. As shown in Fig. 5a, the nanocomposite membranes containing moderate ZIF-8 ($\leq$0.02 wt%) exhibit higher methanol permeance without sacrificing the rejection

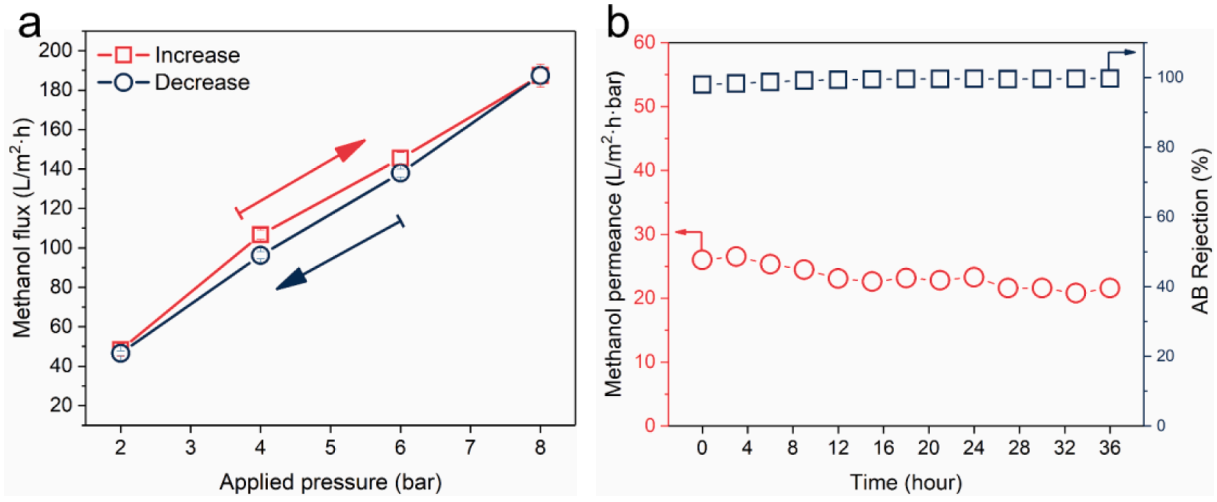

Fig. 6. Performance variation of the MPN/ZIF-8-2 membrane under (a) different pressures and (b) operation time. AB methanol solution (50 mg/L) is used as feed and the operation pressure is fixed at 4 bar for the long-term test.

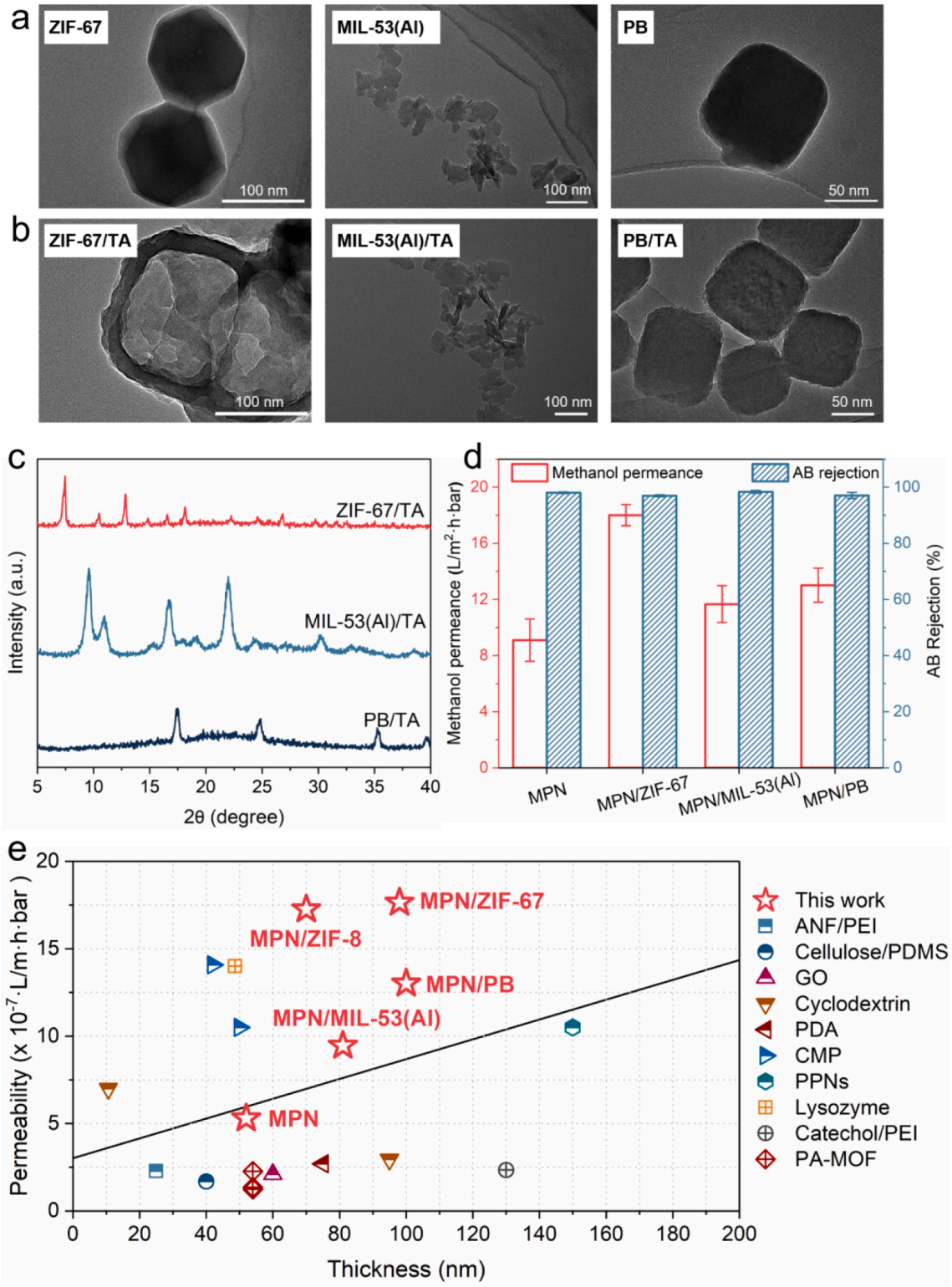

Fig. 7. TEM images of the synthesized ZIF-67, MIL-53(Al), and PB nanoparticles (a) before and (b) after TA modification. (c) XRD spectra of ZIF-67/TA, PB/TA and MIL-53(Al)/TA. (d) OSN performances of MPN membrane and different nanocomposite membranes. (e) Plots of permeability versus selective layer thickness for OSN membranes in this work and literatures.

performance for RB compared with the MPN membrane. This is because the hollow ZIF-8 nanoparticles provide affluent mass transfer channels for the selective layer while maintaining good interface compatibility with the MPN matrix, resulting in decreased hydraulic resistance for solvents. However, the overloading of ZIF-8 (0.03 wt% and 0.04 wt%) will lead to declined RB rejection mainly ascribed to the loose structure of the MPN/ZIF-8 layer. It can be observed in Figure S7 and S8, the membrane surface becomes rough with the ZIF-8 amount increasing while the layer thickness changes little. However, the pore size of MPN/ZIF-8 layers increases with ZIF-8 amount proved by the deteriorated rejection ability of MPN/ZIF-8 membranes towards various dyes, indicating looser structure of the selective layer (Figure S9). So the additive

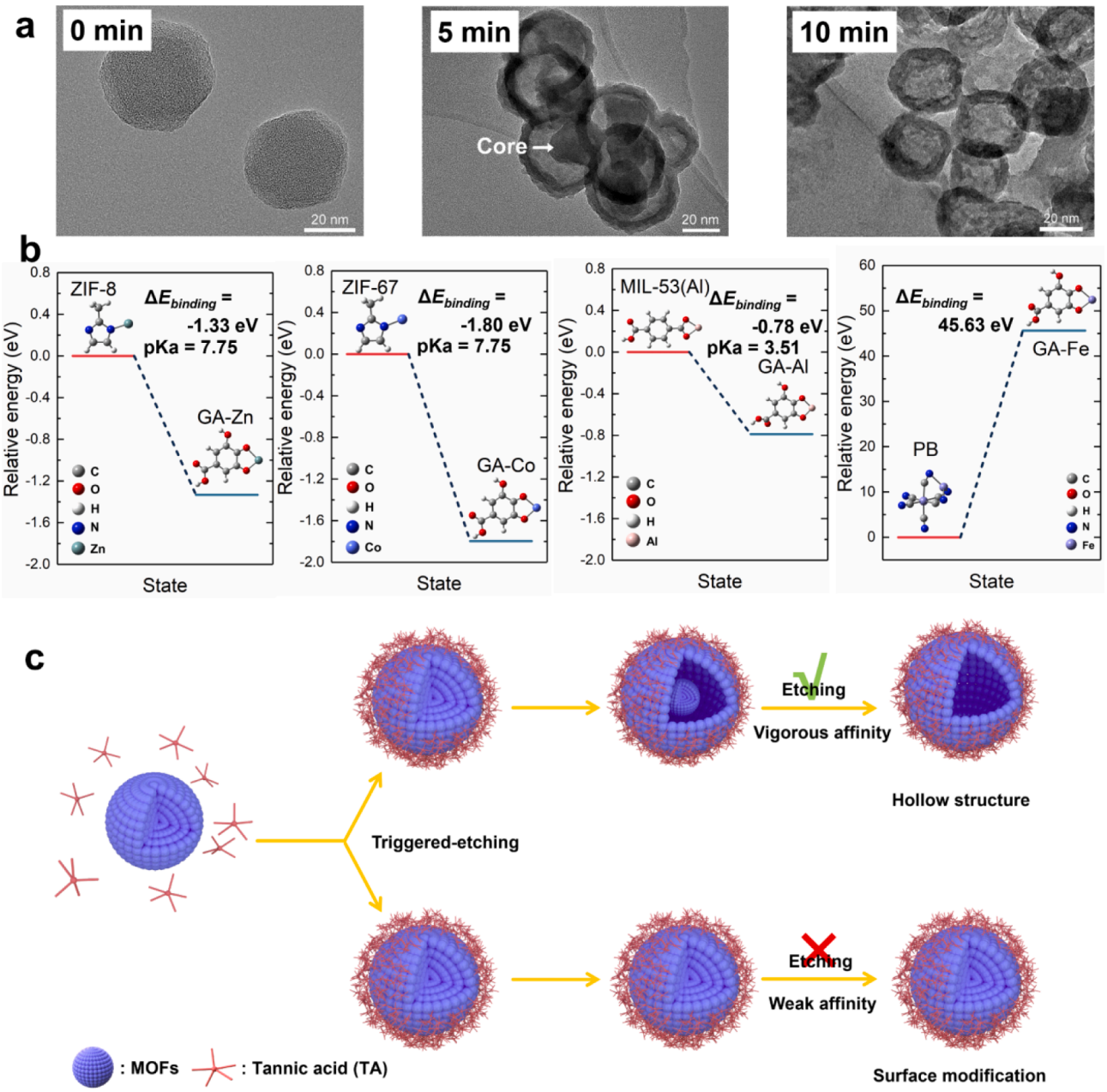

Fig. 8. (a) TEM images of ZIF-8/TA nanoparticles with different etching time. (b) Calculated relative binding energies between different metal ions and organic ligands. (c) Schematic illustration of the etching process.

amount of ZIF-8 is optimized at 0.02 wt% for further investigation. As shown in Fig. 5b, both of the methanol permeance and RB rejection increase when deposition time vary from 1 h to 2 h, attributed to the formation of a defect-free MPN/ZIF-8 layer. However, the OSN performance degrades as the deposition time is further prolonged. This is because the ZIF-8 amount loaded in the MPN/ZIF-8 layer would increases with deposition time, leading to loose structure and thus declined RB rejection (Figure S10, Figure S11, and Table S1). Therefore, 0.02 wt% of ZIF-8 and 2 h of deposition time are adopted as optimized fabrication conditions.

The optimized MPN/ZIF-8 membranes with a molecular weight cutoff (MWCO) of 1040 Da were applied for filtrating different organic solutions (Fig. 5c). These membranes exhibits high rejection (>99 %) for AB (MW = 1298 g·mol^{-1}, 1.95 × 2.17 nm) but low rejection (<55 %) for MO (MW = 327 g·mol^{-1}, 1.47 × 0.43 nm), indicating good selectivity for organic molecules with different sizes (Figure S12, and Table S2). As the dye adsorption capacity of MPN/ZIF-8-2 membranes is relatively low, the rejection performance mainly generates from their small pore size of about 1.26 nm with reasonable distribution (Figure S13 and Figure S14).

The effect of organic solvents on the membrane permeance was also investigated. As shown in Fig. 5d, the MPN/ZIF-8-2 membrane reveals higher permeance than the MPN membrane for all organic solvents attributed to the embedded hollow ZIF-8. As the membrane permeance order for organic solvents depends on the physical parameters of organic solvents, the methanol permeance is the highest among all of the solvents due to the lower molar diameter (d_m), viscosity (η) and higher dipole forces (δ_p) (Table S3). Particularly, the MPN/ZIF-8-2 membrane exhibits an extremely high methanol permeance of 24.7 L·m^{-2}·h^{-1}·bar^{-1}, indicating a spectacular improvement of 270% compared with the MPN membrane (9.1 L·m^{-2}·h^{-1}·bar^{-1}). This is significantly important for enhancing the separation efficiency of OSN.

The structure and performance stability of the MPN/ZIF-8-2

membranes were also evaluated. As shown in Fig. 6a, the MPN/ZIF-8-2 membrane shows little permeance variation under the cycle of pressurization and decompression. Furthermore, the MPN/ZIF-8-2 membrane also exhibits stable methanol permeance (21.6 $L{\cdot}m^{-2}{\cdot}h^{-1}{\cdot}bar^{-1}$) as well as dye rejection (>99%) during a long-term continuous filtration of 36 h (Fig. 6b). These results reveal excellent structural and chemical stability of the prepared nanocomposite membranes, which is of great importance for their practical applications.

To further explore the universality of this aqueous strategy, ZIF-67, PB and MIL-53(Al) are also adopted to fabricate nanocomposite membranes with TA-Fe^{II}. TEM images show that the ZIF-67 nanoparticles are etched to a hollow structure by TA, while PB and MIL-53(Al) maintain the original structure (Fig. 7a and 7b). The diagnostic diffraction peaks in XRD spectra of the MOFs are consistent with that of the corresponding standard samples, indicating the well preserved crystal structures (Fig. 7c and Figure S15). As shown in Figure S16, the three MOFs can be deposited onto substrate surface with MPN to form MPN/MOFs nanocomposite layers with thickness of around 100 nm, which is also confirmed by the EDX elemental mapping results (Figure S17). Benefiting from the hollow structure of ZIF-67, the MPN/ZIF-67 nanocomposite membrane exhibits a remarkable improvement in methanol permeance from 9.1 $L{\cdot}m^{-2}{\cdot}h^{-1}{\cdot}bar^{-1}$ to 18.0 $L{\cdot}m^{-2}{\cdot}h^{-1}{\cdot}bar^{-1}$ when compared with MPN membrane (Fig. 7d). Meanwhile, the MPN/MIL-53 (Al) and MPN/PB membranes also reveal better permeability for methanol ascribed to the porous nanofillers. As the intrinsic permeability ($\times10^{-7}{\cdot}L{\cdot}m^{-1}{\cdot}h^{-1}{\cdot}bar^{-1}$) can be used to characterize the mass transfer efficiency of membranes, we comprehensively summarize the methanol permeance, dye rejection and membrane thickness of advanced OSN membranes here (Table S5, membranes with MWCO above 500 are considered). [54] From Fig. 7e, the prepared MPN/MOFs nanocomposite membranes in this work, especially the membranes containing hollow MOFs, show higher permeability than the currently reported OSN membranes, demonstrating the superiority of the novel nanocomposite membranes in OSN applications.

Both experiments and simulations were conducted in order to get deeper insight into the etching process. As shown in Fig. 8a, ZIF-8 nanoparticles vary from homogeneously porous structure to eggshell structure, and finally become hollow with the etching time increasing to 10 min. This result implies that the TA molecules can firstly attach to the surface of ZIF-8 through coordination interaction with the exposed Zn centers and stabilize the integral crystal morphology. The pores on ZIF-8 surface (0.34 nm) impede the TA molecules (around 1 nm) from further entering inside the crystals while permitting the protons in TA solutions to invade the inner and dissolve the cores. [55] As a result, the ZIF-8 nanoparticles can be etched into a hollow structure (Fig. 8c). Additionally, the DFT calculation was employed to estimate the etching possibility of different MOFs through the binding energies of different organic ligands with metal ions. As shown in Fig. 8b, the $\Delta E_{binding}$ values between phenolic molecules and Zn^{II}, Co^{II} and Al^{III} are lower than that between organic ligands and metal ions of the original MOFs. This means that TA molecules can replace the organic ligands of MOFs spontaneously during the modification process. However, it should be noticed that the imidazole ligands in ZIF-8 and ZIF-67 possess higher pK_a (7.75) than that of the carboxylic acid ligands in MIL-53(Al) (pK_a = 3.51), suggesting higher affinity between imidazole groups and protons. [56,57] Therefore, in acidic solutions, imidazole-based MOFs are prone to dissolve while carboxylic acid-based MOFs can maintain stable. [58] And for PB, its intrinsic high binding energy and good stability in the aqueous system make it difficult to be etched under acidic conditions. [59] It can be demonstrated that the TA-Fe^{III} MPN matrix could form nanocomposite structures with different MOFs though the formation of hollow MOFs depends on the affinity between protons and organic ligands (Fig. 8c).

4. Conclusion

In summary, a novel nanocomposite membrane was successfully prepared via an aqueous deposition of MPN (TA-Fe^{II}) with *in-situ* etched hollow MOFs on a porous substrate. The permeability of the nanocomposite membranes to different organic solvents has been improved significantly without sacrificing the rejection performance ascribed to the extra transfer channels in hollow MOFs and the excellent interface compatibility between the MPN matrix and MOFs. Especially, the methanol permeance of the optimized nanocomposite membranes increases from 9.1 $L{\cdot}m^{-2}{\cdot}h^{-1}{\cdot}bar^{-1}$ to 24.7 $L{\cdot}m^{-2}{\cdot}h^{-1}{\cdot}bar^{-1}$, achieving a distinguished improvement of 270% compared with the neat MPN membranes. Various MOFs are also proved to construct MPN/MOFs nanocomposite membranes by this one-step aqueous deposition strategy, and exhibit different degrees of performance improvement. The *in-situ* etching mechanism of MOFs is further clarified by DFT calculation. We believe that this work will pave a new way for the preparation of hollow MOFs as nanofillers, as well as a new-generation high-performance OSN membranes.

Declaration of Competing Interest

The authors declare that they have no known competing financial interests or personal relationships that could have appeared to influence the work reported in this paper.

Acknowledgement

The authors thank financial support from the National Natural Science Foundation of China (22108030), Natural Science Foundation of Shanghai (22ZR1401500), Shanghai Sailing Program (19YF1400900), China Postdoctoral Science Foundation (2021M702475), and the Shanghai Pujiang Program (21PJ1413000).

Appendix A. Supplementary data

Supplementary data to this article can be found online at https://doi.org/10.1016/j.cej.2022.135289.

References

[1] R.P. Lively, D.S. Sholl, From water to organics in membrane separations, Nat. Mater. 16 (3) (2017) 276–279, https://doi.org/10.1038/nmat4860.
[2] L. Peeva, J. DaSilvaBurgal, Z. Heckenast, F. Brazy, F. Cazenave, A. Livingston, Continuous consecutive reactions with inter-reaction solvent exchange by membrane separation, Angew. Chem. Int. Ed. 55 (43) (2016) 13576–13579.
[3] Y. Li, Z. Guo, S. Li, B. Van der Bruggen, Interfacially polymerized thin-film composite membranes for organic solvent nanofiltration, Adv. Mater. Interfaces 8 (3) (2021) 2001671, https://doi.org/10.1002/admi.202001671.
[4] S. Schlüter, K.U. Künnemann, M. Freis, T. Roth, D. Vogt, J.M. Dreimann, M. Skiborowski, Continuous co-product separation by organic solvent nanofiltration for the hydroaminomethylation in a thermomorphic multiphase system, Chem. Eng. J. 409 (2021), 128219, https://doi.org/10.1016/j.cej.2020.128219.
[5] Q. Liu, S. Xu, S. Xiong, M. Yi, Y. Wang, Coordination-crosslinked polyimide supported membrane for ultrafast molecular separation in multi-solvent systems, Chem. Eng. J. 427 (2022), 130941, https://doi.org/10.1016/j.cej.2021.130941.
[6] P. Marchetti, M.F. Jimenez Solomon, G. Szekely, A.G. Livingston, Molecular separation with organic solvent nanofiltration: a critical review, Chem. Rev. 114 (21) (2014) 10735–10806.
[7] J. Campbell, G. Székely, R.P. Davies, D.C. Braddock, A.G. Livingston, Fabrication of hybrid polymer/metal organic framework membranes: mixed matrix membranes versus in situ growth, J. Mater. Chem. A 2 (24) (2014) 9260–9271, https://doi.org/10.1039/C4TA00628C.
[8] S. Karan, Z. Jiang, A.G. Livingston, Sub-10 nm polyamide nanofilms with ultrafast solvent transport for molecular separation, Science 348 (6241) (2015) 1347–1351, https://doi.org/10.1126/science.aaa5058.
[9] G.L. Jadav, P.S. Singh, Synthesis of novel silica-polyamide nanocomposite membrane with enhanced properties, J. Membr. Sci. 328 (1) (2009) 257–267, https://doi.org/10.1016/j.memsci.2008.12.014.
[10] S.G. Kim, D.H. Hyeon, J.H. Chun, B.-H. Chun, S.H. Kim, Nanocomposite poly (arylene ether sulfone) reverse osmosis membrane containing functional zeolite

nanoparticles for seawater desalination, J. Membr. Sci. 443 (2013) 10–18, https://doi.org/10.1016/j.memsci.2013.03.065.
[11] G.S. Lai, W.J. Lau, P.S. Goh, A.F. Ismail, Y.H. Tan, C.Y. Chong, R. Krause-Rehberg, S. Awad, Tailor-made thin film nanocomposite membrane incorporated with graphene oxide using novel interfacial polymerization technique for enhanced water separation, Chem. Eng. J. 344 (2018) 524–534, https://doi.org/10.1016/j.cej.2018.03.116.
[12] C.Y. Chuah, K. Goh, Y. Yang, H. Gong, W. Li, H.E. Karahan, M.D. Guiver, R. Wang, T.-H. Bae, Harnessing filler materials for enhancing biogas separation membranes, Chem. Rev. 118 (18) (2018) 8655–8769, https://doi.org/10.1021/acs.chemrev.8b0009110.1021/acs.chemrev.8b00091.s001.
[13] X. Cheng, X.U. Jiang, Y. Zhang, C.H. Lau, Z. Xie, D. Ng, S.J.D. Smith, M.R. Hill, L. U. Shao, Building additional passageways in polyamide membranes with hydrostable metal organic frameworks to recycle and remove organic solutes from various solvents, ACS Appl. Mater. Interfaces 9 (44) (2017) 38877–38886, https://doi.org/10.1021/acsami.7b0737310.1021/acsami.7b07373.s001.
[14] Y.-L. Ji, B.-X. Gu, S.-J. Xie, M.-J. Yin, W.-J. Qian, Q. Zhao, W.-S. Hung, K.-R. Lee, Y. Zhou, Q.-F. An, C.-J. Gao, Superfast water transport zwitterionic polymeric nanofluidic membrane reinforced by metal-organic frameworks, Adv. Mater. 33 (38) (2021) 2102292, https://doi.org/10.1002/adma.202102292.
[15] C. Li, J. Li, W.-H. Zhang, N. Wang, S. Ji, Q.-F. An, Enhanced permeance for PDMS organic solvent nanofiltration membranes using modified mesoporous silica nanoparticles, J. Membr. Sci. 612 (2020), 118257, https://doi.org/10.1016/j.memsci.2020.118257.
[16] X.-Y. Ma, T.-T. Fan, G. Wang, Z.-H. Li, J.-H. Lin, Y.-Z. Long, High performance GO/MXene/PPS composite filtration membrane for dye wastewater treatment under harsh environmental conditions, Compos. Commun. 29 (2022), 101017, https://doi.org/10.1016/j.coco.2021.101017.
[17] Q. Lan, N. Yan, H. Yang, Y. Wang, Nanocomposite block copolymer membranes with enhanced permeance and robustness by carbon nanotube doping, Compos. Commun. 29 (2022), 101025, https://doi.org/10.1016/j.coco.2021.101025.
[18] M.S. Denny, J.C. Moreton, L. Benz, S.M. Cohen, Metal-organic frameworks for membrane-based separations, J. Mater. Chem. A 1 (12) (2016) 16078, https://doi.org/10.1038/natrevmats.2016.78.
[19] X. Li, Y. Liu, J. Wang, J. Gascon, J. Li, B. Van der Bruggen, Metal-organic frameworks based membranes for liquid separation, Chem. Soc. Rev. 46 (23) (2017) 7124–7144, https://doi.org/10.1039/C7CS00575J.
[20] J. Cui, A. Xie, Y. Liu, C. Xue, J. Pan, Fabrication of multi-functional imprinted composite membrane for selective tetracycline and oil-in-water emulsion separation, Compos. Commun. 28 (2021), 100985, https://doi.org/10.1016/j.coco.2021.100985.
[21] E. Doustkhah, R. Hassandoost, A. Khataee, R. Luque, M.H.N. Assadi, Hard-templated metal-organic frameworks for advanced applications, Chem. Soc. Rev. 50 (5) (2021) 2927–2953, https://doi.org/10.1039/C9CS00813F.
[22] M.M. Zagho, M.K. Hassan, M. Khraisheh, M.A.A. Al-Maadeed, S. Nazarenko, A review on recent advances in CO_2 separation using zeolite and zeolite-like materials as adsorbents and fillers in mixed matrix membranes (MMMs), Chem. Eng. J. Adv. 6 (2021), 100091, https://doi.org/10.1016/j.ceja.2021.100091.
[23] T. Qiu, S. Gao, Z. Liang, D.-G. Wang, H. Tabassum, R. Zhong, R. Zou, Pristine hollow metal-organic frameworks: Design, synthesis and application, Angew. Chem. Int. Ed. 60 (32) (2021) 17314–17336, https://doi.org/10.1002/anie.202012699.
[24] S. Sorribas, P. Gorgojo, C. Téllez, J. Coronas, A.G. Livingston, High flux thin film nanocomposite membranes based on metal-organic frameworks for organic solvent nanofiltration, J. Am. Chem. Soc. 135 (40) (2013) 15201–15208, https://doi.org/10.1021/ja407665w.
[25] J. Zhu, L. Qin, A. Uliana, J. Hou, J. Wang, Y. Zhang, X. Li, S. Yuan, J. Li, M. Tian, J. Lin, B. Van der Bruggen, Elevated performance of thin film nanocomposite membranes enabled by modified hydrophilic mofs for nanofiltration, ACS Appl. Mater. Interfaces 9 (2) (2017) 1975–1986, https://doi.org/10.1021/acsami.6b1441210.1021/acsami.6b14412.s001.
[26] B. Sasikumar, S. Bisht, G. Arthanareeswaran, A.F. Ismail, M.H.D. Othman, Performance of polysulfone hollow fiber membranes encompassing ZIF-8, SiO_2/ZIF-8, and amine-modified SiO_2/ZIF-8 nanofillers for CO_2/CH_4 and CO_2/N_2 gas separation, Sep. Purif. Technol. 264 (2021), 118471, https://doi.org/10.1016/j.seppur.2021.118471.
[27] H. Sun, B. Tang, P. Wu, Development of hybrid ultrafiltration membranes with improved water separation properties using modified superhydrophilic metal-organic framework nanoparticles, ACS Appl. Mater. Interfaces 9 (25) (2017) 21473–21484, https://doi.org/10.1021/acsami.7b0550410.1021/acsami.7b05504.s001.
[28] J. Dechnik, J. Gascon, C.J. Doonan, C. Janiak, C.J. Sumby, Mixed-matrix membranes, Angew. Chem. Int. Ed. 56 (32) (2017) 9292–9310, https://doi.org/10.1002/anie.201701109.
[29] Z. Wang, D. Wang, S. Zhang, L. Hu, J. Jin, Interfacial design of mixed matrix membranes for improved gas separation performance, Adv. Mater. 28 (17) (2016) 3399–3405, https://doi.org/10.1002/adma.201504982.
[30] R. Wang, X. Zhao, N. Jia, L. Cheng, L. Liu, C. Gao, Superwetting oil/water separation membrane constructed from in situ assembled metal-phenolic networks and metal-organic frameworks, ACS Appl. Mater. Interfaces 12 (8) (2020) 10000–10008, https://doi.org/10.1021/acsami.9b2208010.1021/acsami.9b22080.s001.
[31] Z. Liao, X. Fang, J. Xie, Q. Li, D. Wang, X. Sun, L. Wang, J. Li, Hydrophilic hollow nanocube-functionalized thin film nanocomposite membrane with enhanced nanofiltration performance, ACS Appl. Mater. Interfaces 11 (5) (2019) 5344–5352, https://doi.org/10.1021/acsami.8b1912110.1021/acsami.8b19121.s001.
[32] H. Wang, W. Zhu, Y. Ping, C. Wang, N. Gao, X. Yin, C. Gu, D. Ding, C.J. Brinker, G. Li, Controlled fabrication of functional capsules based on the synergistic interaction between polyphenols and MOFs under weak basic condition, ACS Appl. Mater. Interfaces 9 (16) (2017) 14258–14264, https://doi.org/10.1021/acsami.7b0178810.1021/acsami.7b01788.s001.
[33] M. Hu, Y. Ju, K. Liang, T. Suma, J. Cui, F. Caruso, Void engineering in metal-organic frameworks via synergistic etching and surface functionalization, Adv. Funct. Mater. 26 (32) (2016) 5827–5834, https://doi.org/10.1002/adfm.201601193.
[34] X. Cheng, Z. Jiang, X. Cheng, H. Yang, L. Tang, G. Liu, M. Wang, H. Wu, F. Pan, X. Cao, Water-selective permeation in hybrid membrane incorporating multi-functional hollow ZIF-8 nanospheres, J. Membr. Sci. 555 (2018) 146–156, https://doi.org/10.1016/j.memsci.2018.03.024.
[35] H. Ejima, J.J. Richardson, F. Caruso, Metal-phenolic networks as a versatile platform to engineer nanomaterials and biointerfaces, NANO Today 12 (2017) 136–148, https://doi.org/10.1016/j.nantod.2016.12.012.
[36] H. Ejima, J.J. Richardson, K. Liang, J.P. Best, M.P. van Koeverden, G.K. Such, J. Cui, F. Caruso, One-step assembly of coordination complexes for versatile film and particle engineering, Science 341 (6142) (2013) 154–157.
[37] L. Fan, Y. Ma, Y. Su, R. Zhang, Y. Liu, Q. Zhang, Z. Jiang, Green coating by coordination of tannic acid and iron ions for antioxidant nanofiltration membranes, RSC Adv. 5 (130) (2015) 107777–107784, https://doi.org/10.1039/C5RA23490E.
[38] F. You, Y. Xu, X. Yang, Y. Zhang, L. Shao, Bio-inspired Ni^{2+}-polyphenol hydrophilic network to achieve unconventional high-flux nanofiltration membranes for environmental remediation, Chem. Commun. 53 (45) (2017) 6128–6131, https://doi.org/10.1039/C7CC02411H.
[39] C.-E. Lin, M.-Y. Zhou, W.-S. Hung, B.-K. Zhu, K.-R. Lee, L.-P. Zhu, L.-F. Fang, Ultrathin nanofilm with tailored pore size fabricated by metal-phenolic network for precise and rapid molecular separation, Sep. Purif. Technol. 207 (2018) 435–442, https://doi.org/10.1016/j.seppur.2018.06.077.
[40] Y.-J. Shen, L.-F. Fang, Y. Yan, J.-J. Yuan, Z.-Q. Gan, X.-Z. Wei, B.-K. Zhu, Metal-organic composite membrane with sub-2 nm pores fabricated via interfacial coordination, J. Membr. Sci. 587 (2019), 117146, https://doi.org/10.1016/j.memsci.2019.05.070.
[41] T. Chakrabarty, L. Pérez-Manríquez, P. Neelakanda, K.-V. Peinemann, Bioinspired tannic acid-copper complexes as selective coating for nanofiltration membranes, Sep. Purif. Technol. 184 (2017) 188–194, https://doi.org/10.1016/j.seppur.2017.04.043.
[42] Y. Xiao, D. Guo, T. Li, Q. Zhou, L. Shen, R. Li, Y. Xu, H. Lin, Facile fabrication of superhydrophilic nanofiltration membranes via tannic acid and irons layer-by-layer self-assembly for dye separation, Appl. Surf. Sci. 515 (2020), 146063, https://doi.org/10.1016/j.apsusc.2020.146063.
[43] H. Lee, W.I. Kim, W. Youn, T. Park, S. Lee, T.-S. Kim, J.F. Mano, I.S. Choi, Iron gall ink revisited: In situ oxidation of Fe(II)-tannin complex for fluidic-interface engineering, Adv. Mater. 30 (49) (2018) 1805091, https://doi.org/10.1002/adma.201805091.
[44] Q.-Z. Zhong, S. Li, J. Chen, K. Xie, S. Pan, J.J. Richardson, F. Caruso, Oxidation-mediated kinetic strategies for engineering metal-phenolic networks, Angew. Chem. Int. Ed. 58 (36) (2019) 12563–12568, https://doi.org/10.1002/anie.201907666.
[45] J. Sánchez-Laínez, B. Zornoza, S. Friebe, J. Caro, S. Cao, A. Sabetghadam, B. Seoane, J. Gascon, F. Kapteijn, C. Le Guillouzer, G. Clet, M. Daturi, C. Téllez, J. Coronas, Influence of ZIF-8 particle size in the performance of polybenzimidazole mixed matrix membranes for pre-combustion CO_2 capture and its validation through interlaboratory test, J. Membr. Sci. 515 (2016) 45–53, https://doi.org/10.1016/j.memsci.2016.05.039.
[46] J. Qian, F. Sun, L. Qin, Hydrothermal synthesis of zeolitic imidazolate framework-67 (ZIF-67) nanocrystals, Mater. Lett. 82 (2012) 220–223, https://doi.org/10.1016/j.matlet.2012.05.077.
[47] L. Zhang, H.B. Wu, S. Madhavi, H.H. Hng, X.W. Lou, Formation of Fe_2O_3 microboxes with hierarchical shell structures from metal-organic frameworks and their lithium storage properties, J. Am. Chem. Soc. 134 (42) (2012) 17388–17391, https://doi.org/10.1021/ja307475c.
[48] Y. Lv, H.-C. Yang, H.-Q. Liang, L.-S. Wan, Z.-K. Xu, Nanofiltration membranes via co-deposition of polydopamine/polyethylenimine followed by cross-linking, J. Membr. Sci. 476 (2015) 50–58, https://doi.org/10.1016/j.memsci.2014.11.024.
[49] W.J. Hehre, R. Ditchfield, J.A. Pople, Self-Consistent Molecular Orbital Methods. XII. Further Extensions of Gaussian-Type Basis Sets for Use in Molecular Orbital Studies of Organic Molecules, The Journal of Chemical Physics 56(5) 56 (5) (1972) 2257–2261, https://doi.org/10.1063/1.1677527.
[50] A.D. Becke, Density-functional thermochemistry. III. The role of exact exchange, J. Chem. Phys. 98 (7) (1993) 5648–5652.
[51] P.C. Hariharan, J.A. Pople, The influence of polarization functions on molecular orbital hydrogenation energies, Theor. Chim. Acta 28 (3) (1973) 213–222, https://doi.org/10.1007/BF00533485.
[52] S. Grimme, S. Ehrlich, L. Goerigk, Effect of the damping function in dispersion corrected density functional theory, J. Comput. Chem. 32 (7) (2011) 1456–1465, https://doi.org/10.1002/jcc.21759.
[53] A. Avdeef, S.R. Sofen, T.L. Bregante, K.N. Raymond, Coordination chemistry of microbial iron transport compounds. 9. Stability constants for catechol models of enterobactin, J. Am. Chem. Soc. 100 (17) (1978) 5362–5370.
[54] M.-B. Wu, F. Yang, J. Yang, Q.i. Zhong, V. Körstgen, P. Yang, P. Müller-Buschbaum, Z.-K. Xu, Lysozyme membranes promoted by hydrophobic substrates for ultrafast and precise organic solvent nanofiltration, NANO Lett. 20 (12) (2020) 8760–8767,

https://doi.org/10.1021/acs.nanolett.0c0363210.1021/acs.nanolett.0c03632.s001.

[55] K.S. Park, Z. Ni, A.P. Côté, J.Y. Choi, R. Huang, F.J. Uribe-Romo, H.K. Chae, M. O'Keeffe, O.M. Yaghi, Exceptional chemical and thermal stability of zeolitic imidazolate frameworks, Proc. Natl. Acad. Sci. U.S.A. 103 (27) (2006) 10186–10191, https://doi.org/10.1073/pnas.0602439103.

[56] J.D. Roberts Determination of organic structures by physical methods J. Am. Chem. Soc. 78 4 1956 886 886 10.1021/ja01585a060.

[57] T.C. Bruice, G.L. Schmir, Imidazole Catalysis. II. The Reaction of Substituted Imidazoles with Phenyl Acetates in Aqueous Solution, J. Am. Chem. Soc. 80 (1) (1958) 148–156.

[58] S. Yuan, L. Feng, K. Wang, J. Pang, M. Bosch, C. Lollar, Y. Sun, J. Qin, X. Yang, P. Zhang, Q. Wang, L. Zou, Y. Zhang, L. Zhang, Y. Fang, J. Li, H.-C. Zhou, Stable metal-organic frameworks: Design, synthesis, and applications, Adv. Mater. 30 (37) (2018) 1704303, https://doi.org/10.1002/adma.201704303.

[59] L.-P. Wang, P.-F. Wang, T.-S. Wang, Y.-X. Yin, Y.-G. Guo, C.-R. Wang, Prussian blue nanocubes as cathode materials for aqueous Na-Zn hybrid batteries, J. Power Sources 355 (2017) 18–22, https://doi.org/10.1016/j.jpowsour.2017.04.049.